Structural Durability & Health Monitoring

Tech Science Press

https://doi.org/10.32604/sdhm.2026.080465

ARTICLE

An Integrated Simulation Framework for Reliability Assessment of Bolted Joints in Lightweight High-Speed Train Battery Housings

Lin Zang[1], Muhammad Fadhil Marsani[2,*], Caiyan Long[1,2,*] and Yongping Yu[3]

[1]School of Integrated Circuits and New Energy, Guangzhou College of Technology and Business, Guangzhou, China
[2]School of Mathematical Sciences, Universiti Sains Malaysia, Penang, Malaysia
[3]School of Construction Engineering, Jilin University, Changchun, China

*Corresponding Authors: Muhammad Fadhil Marsani. Email: fadhilmarsani@usm.my; Caiyan Long. Email: longcaiyan@student.usm.my

Received: 10 February 2026; Accepted: 17 April 2026; Published: 30 June 2026

ABSTRACT: To bridge the gap between isolated structural and connection analyses in lightweight rail vehicle design, this study establishes an integrated modelling-simulation-verification framework. This integrated framework, developed via parametric FE modelling, multi-axial load simulation (per DIN EN 12663 & BS 7608), and standards-based verification, was applied to a specific housing design. Key results: (1) Under vertical ±3 g static loads, the tray experiences the maximum equivalent stress of 186.6 MPa, yielding a safety factor of 1.1 against the yield strength, which satisfies the minimum requirement ($s_1 \geq 1.15$) of the DIN EN 12663 standard. (2) Under fatigue spectrum, critical stress amplitudes are 39.38 MPa (lifting seat) and 37.87 MPa (frame), yielding fatigue safety factors of 2.54 and 2.64 (BS 7608 Class B). For the reliability assessment of similar rail transit equipment. The demonstrated framework effectively bridges the gap between isolated structural and connection analyses, providing a systematic tool for lightweight, reliable design. The framework provides validated design data and a reusable methodology for lightweight rail equipment.

KEYWORDS: High-speed train; battery housing; finite element analysis; structural reliability; bolted connection; fatigue life; lightweight structure; dynamic load; safety factor

1 Introduction

As the operational velocities and operational lifespans of modern high-speed railway networks continue to increase, ensuring the structural reliability of on-board equipment has become an engineering imperative dictated by rigorous international standards [1,2]. The under-slung battery housing, operating as a critical auxiliary power unit, ensures uninterrupted emergency power for train start-up and primary control systems. During transit, this housing is continuously subjected to stochastic, multi-axial mechanical loads arising from track irregularities and aerodynamic buffeting [3]. These sustained dynamic excitations propagate through the vehicle carbody, rendering the battery housing susceptible to structural fatigue, localized plastic deformation, and, crucially, the progressive loosening or complete fracture of its bolted connections [4,5]. Consequently, deploying high-fidelity finite element (FE) modeling to systematically map the elastodynamic response of these components under complex operational spectra is a critical prerequisite in contemporary rail vehicle design [6–8].

Static strength analysis forms the baseline for assessing structural load-bearing capacity and has been extensively documented for rail equipment enclosures using traditional FE techniques [6–10]. However, for

under-slung structures subjected to millions of high-frequency stress cycles, high-cycle fatigue remains the governing failure mechanism, requiring dedicated life assessments [7]. In this context, the accurate mathematical representation of bolted joints becomes highly sensitive; the mechanical stiffness and pre-tension of these fasteners fundamentally alter the local stress tensor and interface contact pressure, phenomena well-documented in classical joint mechanics [5,11], with recent experimental reviews focusing on the energy dissipation of bolted interfaces [12].

Historically, the investigation of train-induced vibrations has been heavily skewed toward civil and environmental engineering—focusing primarily on track-soil-structure interactions, propagation mechanisms, and the attenuation of ground-borne vibrations affecting adjacent infrastructure [13–15]. For instance, recent field testing and predictive modeling have successfully mapped vibration transmission from high-speed and urban rail networks to heritage structures and metro depots [16–19]. While these studies provide a robust theoretical foundation for macroscopic elastodynamics, translating these system-level propagation principles to the localized, component-level reliability of on-board equipment presents a distinct computational challenge that remains inadequately addressed in current literature. Within this dynamic environment, vibration-induced bolt loosening—initially conceptualized by Junker—manifests as a highly non-linear localized failure mode that cannot be accurately captured without resolving the coupled dynamics of the entire assembly.

In standard industrial practice, global housing structures and local connection systems are frequently evaluated sequentially using decoupled computational approaches. This methodological isolation is intrinsically flawed: treating the housing as rigid overestimates joint fatigue life by ignoring transient stress redistribution, whereas evaluating the global structure without resolving joint compliance underestimates localized stiffness penalties. Such approximations inadvertently lead to either non-conservative fatigue life predictions or unnecessary mass penalties through over-engineering.

Recognizing these analytical limitations, this study introduces an integrated "modelling-simulation-verification" computational framework. Utilizing a representative lightweight high-speed train battery housing, this framework simultaneously resolves global structural deformation and localized joint mechanics by integrating: (1) parametric FE modeling of the continuous structure alongside explicit bolted interface representations; (2) comprehensive multi-axial load simulations under extreme static criteria (DIN EN 12663 [20]) and composite fatigue spectra (BS 7608); and (3) systematic, standards-compliant safety verification.

Beyond satisfying immediate mechanical design criteria, this coupled framework aligns directly with the emerging paradigm of transportation infrastructure resilience. Long-term structural deterioration inherently dictates system-level availability [21]. By precisely quantifying the damage accumulation states and fatigue limits of vulnerable bolted joints under realistic operational vibrations, the methodology proposed herein provides the deterministic physical data necessary to evaluate post-disaster recovery functions and broader lifecycle resilience [22]. Ultimately, this research not only validates a specific lightweight equipment design but also formalizes a scalable, physics-informed analytical tool for advancing the reliability of next-generation high-speed rail systems.

2 Finite Element Modelling and Load Definition

2.1 Geometry, Materials, and Coordinate System

This study investigates a high-fidelity numerical representation of a lightweight high-speed train battery housing, prioritizing the mechanical reliability of its bolted interfaces under heterogeneous operational loading conditions. As illustrated in Fig. 1, the housing assembly is integrated into the underslung region of

the vehicle carbody. To ensure consistency with railway kinematic analysis, a global Cartesian coordinate system is defined: the X-axis aligns with the vertical dynamic excitation, while the Y and Z axes correspond to the longitudinal and transverse directions, respectively. The assembly—comprising the housing unit, support framework, and bogie interface—manages a significant inertial payload, with the combined mass of the housing and simulated battery modules totaling approximately 1000 kg. A detailed structural schematic is provided in Fig. 2, highlighting the external aerodynamic cladding (skin) and the removable access door (outer panel).

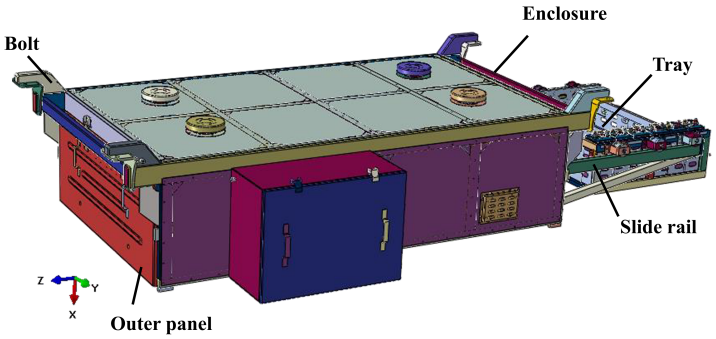

Figure 1: Schematic of battery housing installation and global coordinate system definition.

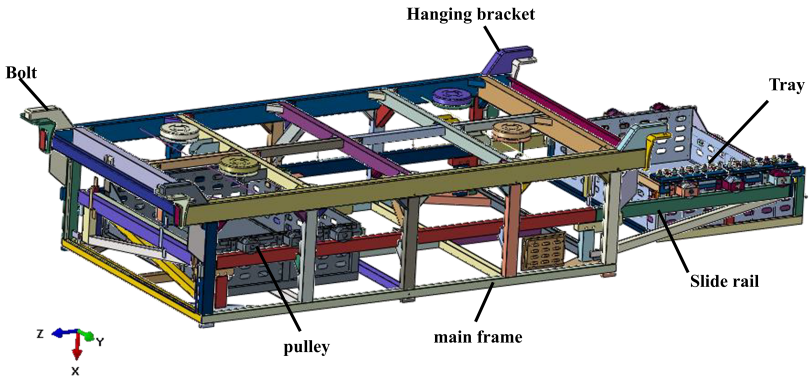

Figure 2: Schematic of the battery housing frame structure.

To meet the stringent weight-reduction and corrosion-resistance requirements of modern rolling stock, the primary structural components are fabricated from 06Cr19Ni10 stainless steel, while mechanical integration is achieved via Grade 8.8 high-strength bolts. The fundamental mechanical properties are detailed in Table 1. Beyond linear elastic parameters, accurately capturing the post-yield response is essential for assessing safety margins under extreme inertial impacts; consequently, the non-linear constitutive behavior—characterized by the true stress-plastic strain hardening curves for both the stainless steel and the fasteners—is explicitly incorporated into the numerical model, as depicted in Fig. 3.

Table 1: Mechanical properties of key component materials.

Component	Material	Young's Modulus (MPa)	Density (kg/m^3)	Poisson's Ratio	Yield Stress (MPa)	Tensile Strength (MPa)
Enclosure	06Cr19Ni10	206,000	7900	0.3	205	515
Slide rail	06Cr19Ni10	206,000	7900	0.3	205	515
Tray	06Cr19Ni10	206,000	7900	0.3	205	515
Outer panel	06Cr19Ni10	206,000	7900	0.3	205	515
Bolt	Grade 8.8	206,000	7900	0.3	640	800

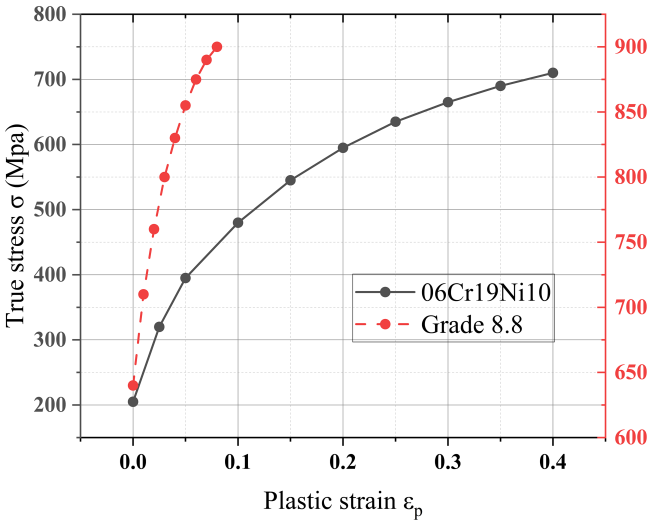

Figure 3: True stress-plastic strain curves for 06Cr19Ni10 and Grade 8.8 bolt.

2.2 Finite Element Model Development

The numerical discretization and subsequent structural evaluations were executed within the Abaqus/Standard environment. This implicit solver was selected specifically for its convergence stability in resolving the complex contact interactions and geometric nonlinearities inherent in large-scale quasi-static assemblies. Furthermore, the availability of high-performance shell formulations and robust bolt-modeling procedures ensures that the load transfer across disparate interfaces remains physically consistent. To maintain an equilibrium between localized stress resolution and global computational economy, the following modeling strategies were adopted:

- Structural Discretization: Thin-walled components, including the mounting brackets, main framework, and cladding panels, were modeled using four-node, reduced-integration shell elements (S4R). Given the high thickness-to-span ratios of these components, the S4R formulation provides an ideal balance by effectively mitigating shear locking while preserving accuracy in large-displacement regimes.
- Bolted Connection Abstraction: Fasteners were represented as simplified axial-flexural members utilizing two-node linear beam elements (B31). Each M10 Grade 8.8 bolt was assigned a corresponding circular cross-section. While this abstraction omits localized thread geometry, it accurately preserves the global stiffness matrix and load propagation paths essential for assembly-level reliability. Bolt pretensioning was implemented via the Bolt Load procedure: an initial clamping force was applied to the

shank in the first analysis step, followed by a "fix-length" constraint in subsequent steps to simulate the sustained clamping effect during external loading. Regarding interface mechanics, the model utilizes Tie constraints to facilitate load transfer between the bolt shank and the structural cladding. Although this approach omits the resolution of localized contact pressure distributions—which would require highly non-linear frictional contact definitions and significantly greater computational cost—it provides a robust representation of the global load propagation path. By enforcing displacement continuity between the fasteners and the housing, the framework effectively captures the resultant axial tension and transverse shear forces. For the purposes of this study, these cross-sectional force vectors are considered more reliable indicators for structural reliability assessment than localized contact stresses, which are often susceptible to numerical singularities at the tie-interfaces in large-scale assemblies.

- Interface Mechanics and Constraints: To facilitate efficient fatigue screening across the 300,000-node assembly, mechanical interfaces were defined using tie constraints. This bonded-interface approach simplifies the non-linear frictional behavior at the joints but ensures a conservative and reliable representation of the primary load-transfer path from the battery mass to the carbody interface.
- Boundary Conditions and Discretization Density: The interfaces between the mounting brackets and the vehicle body were assigned encastre (fully fixed) constraints to simulate the rigid integration with the carbody. The final converged mesh comprised approximately 300,000 elements, providing sufficient discretization density to capture the stress gradients required for both static and high-cycle fatigue assessments. The comprehensive FE assembly is visualized in Fig. 4.

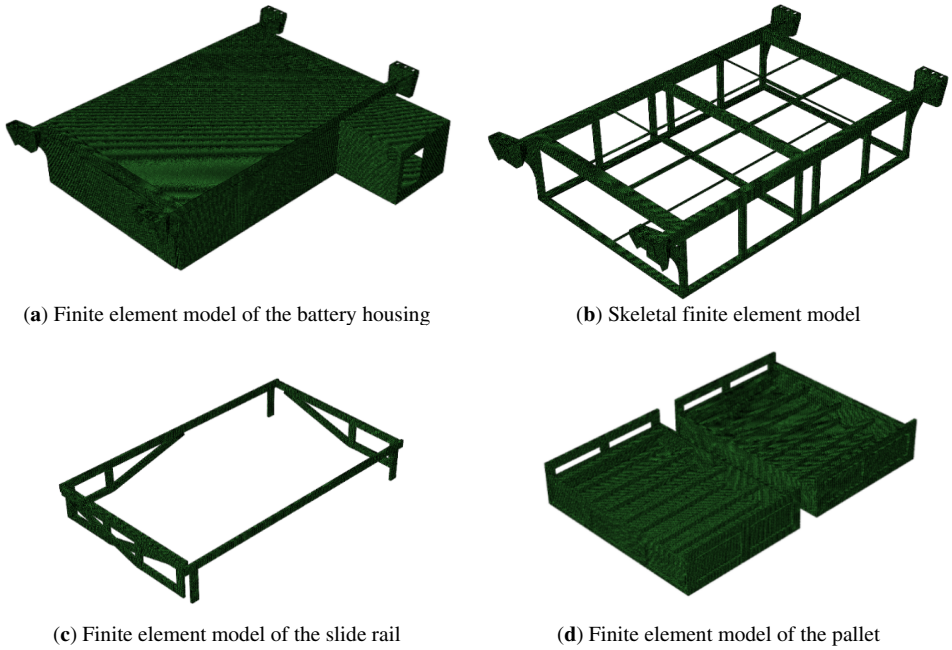

(**a**) Finite element model of the battery housing

(**b**) Skeletal finite element model

(**c**) Finite element model of the slide rail

(**d**) Finite element model of the pallet

Figure 4: Finite element model of the battery housing assembly: (**a**) full assembly, (**b**) frame skeleton, (**c**) slide rail, and (**d**) tray.

2.3 Load Case Definition

Operational safety was evaluated against two distinct loading regimes derived from high-speed rail standards:

- **Static Extremes:** Six static load cases (Table 2) were established in accordance with DIN EN 12663, simulating maximum acceleration, braking, and emergency vertical impacts.
- **Composite Fatigue Spectra:** Eight multi-axial fatigue load cases (F1–F8, Table 3) were defined per BS 7608. These cases represent the stochastic cyclic stressors encountered during long-term operation, encompassing track-induced vibrations and equipment-specific dynamic excitations.

Table 2: Static load cases (DIN EN 12663).

Condition	Acceleration (g)		
	Y (Longitudinal) (g)	Z (Transverse) (g)	X (Vertical) (g)
Condition 1	+3 g	/	1 g
Condition 2	−3 g	/	1 g
Condition 3	/	+1 g	1 g
Condition 4	/	−1 g	1 g
Condition 5	/	/	+3 g
Condition 6	/	/	−3 g

Table 3: Fatigue load cases (BS 7608).

Condition	Acceleration (g)		
	Y (Longitudinal) (g)	Z (Transverse) (g)	X (Vertical) (g)
Condition 1	+0.15 g	+0.15 g	1.15 g
Condition 2	+0.15 g	+0.15 g	0.85 g
Condition 3	+0.15 g	−0.15 g	1.15 g
Condition 4	+0.15 g	−0.15 g	0.85 g
Condition 5	−0.15 g	+0.15 g	1.15 g
Condition 6	−0.15 g	+0.15 g	0.85 g
Condition 7	−0.15 g	−0.15 g	1.15 g
Condition 8	−0.15 g	−0.15 g	0.85 g

2.4 Assessment Criteria

The structural integrity of the housing assembly was validated through a dual-criterion approach: Static Strength (DIN EN 12663): The equivalent stress (σ) must satisfy:

$$\frac{\sigma_c s_1}{R} \leq 1 \, and \, \frac{\sigma_c s_2}{R_m} \leq 1 \tag{1}$$

where R is the material yield strength (205 MPa), R_m is the tensile strength (515 MPa), s_1 = 1.15, and s_2 = 1.5.

Fatigue Design (Based on BS 7608:2014+A1:2015):

The allowable stress amplitude S_a for a Class B welded detail is governed by the S-N curve defined in BS 7608, with a reference stress range (S_r) of 100 MPa at 2×10^6 cycles and a slope m = 4. as listed in Table 4 for Class B base material. For design purposes, a fatigue safety factor γ_f = 1.15 is applied to account for load variability and manufacturing uncertainties, yielding the allowable stress amplitude for design:

$$S_a \leq \frac{100}{1.15} \approx 87.0 \text{ MPa}$$

This simplified expression is commonly adopted in railway structural design practices [10]. The subsequent fatigue screening and life evaluation were performed using the commercial fatigue software fe-safe, based on the FEA results obtained from Abaqus/Standard.

Table 4: Fatigue allowable stress ranges for steel structures and their welded joints.

Grade	Fatigue Strength, Sr (MPa)	m
W	25	3
G	29	3
F2	35	3
F	40	3
E	47	3
D	53	3
C	78	3.5
B	100	4

3 Results and Analysis

The structural performance under the load cases defined in Section 2.3 is evaluated against the criteria in Section 2.4, with the results presented and discussed in the following subsections.

3.1 Static Analysis Results

The stress distributions under three representative static load cases (Condition 1: +1 g vertical; Condition 3: ±1 g lateral; Condition 6: −3 g vertical) are presented in Figs. 5–7, respectively.

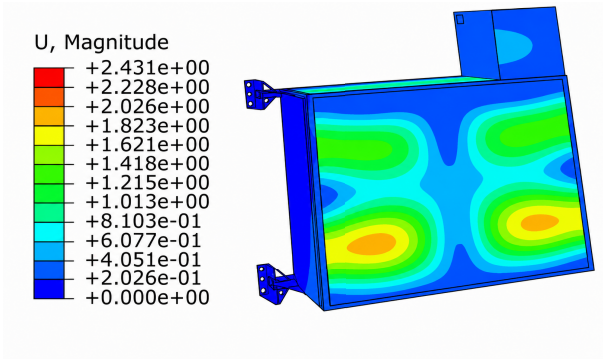

(**a**) overall deformation

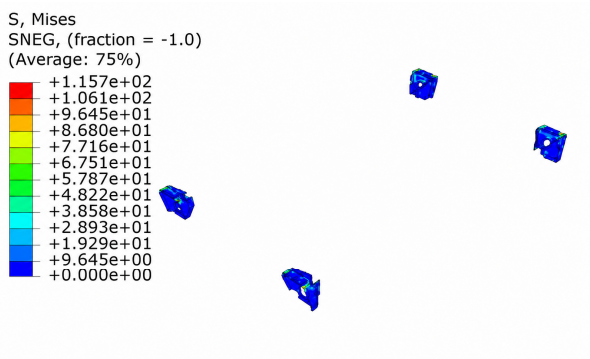

(**b**) lifting seat stress

Figure 5: (Continued)

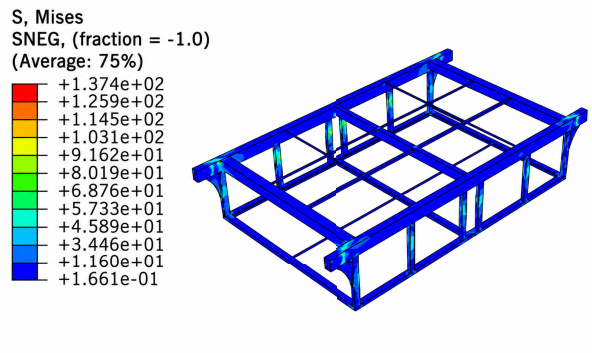

(**c**) frame stress

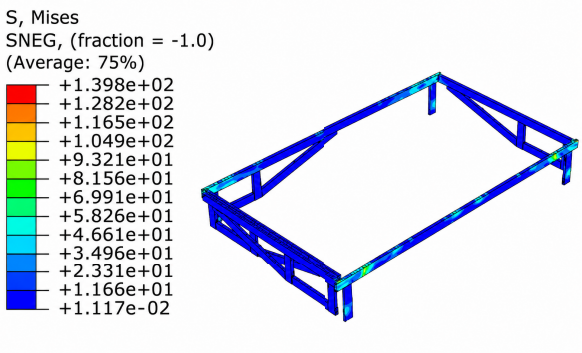

(**d**) slide rail stress

Figure 5: Stress contours and deformation under static Condition 1 (+1 g vertical): (**a**) overall deformation, (**b**) stress at lifting seat, (**c**) stress at frame, (**d**) stress at slide rail. The maximum stress (115.7 MPa) is located at the lifting seat.

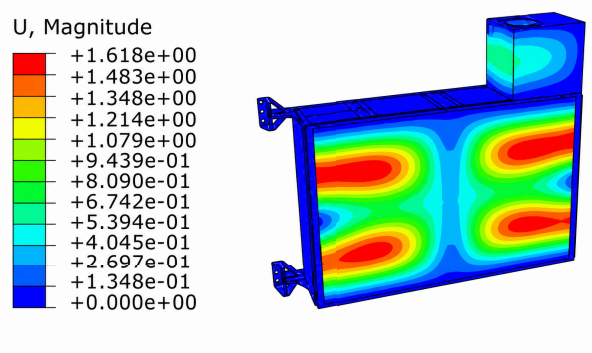

(**a**) overall deformation

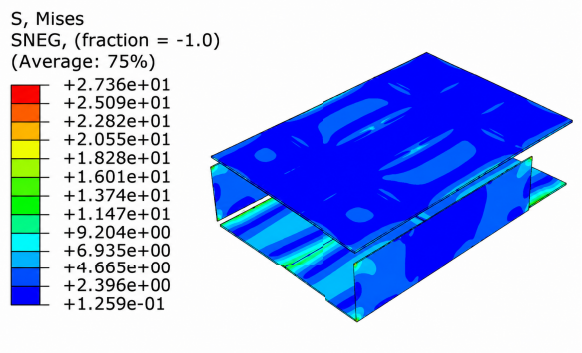

(**b**) skin stress

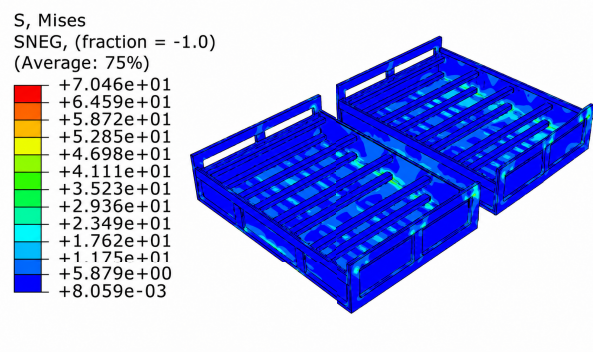

(**c**) tray stress

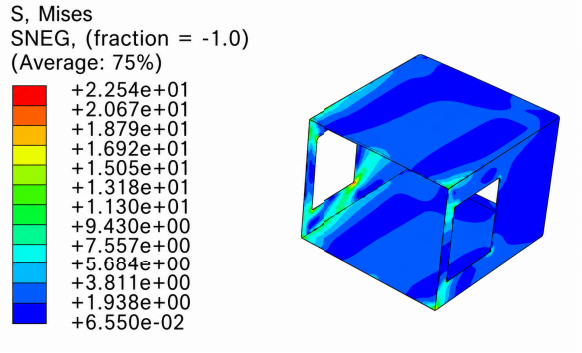

(**d**) junction box stress

Figure 6: Stress contours and deformation under static Condition 3 (±1 g lateral).

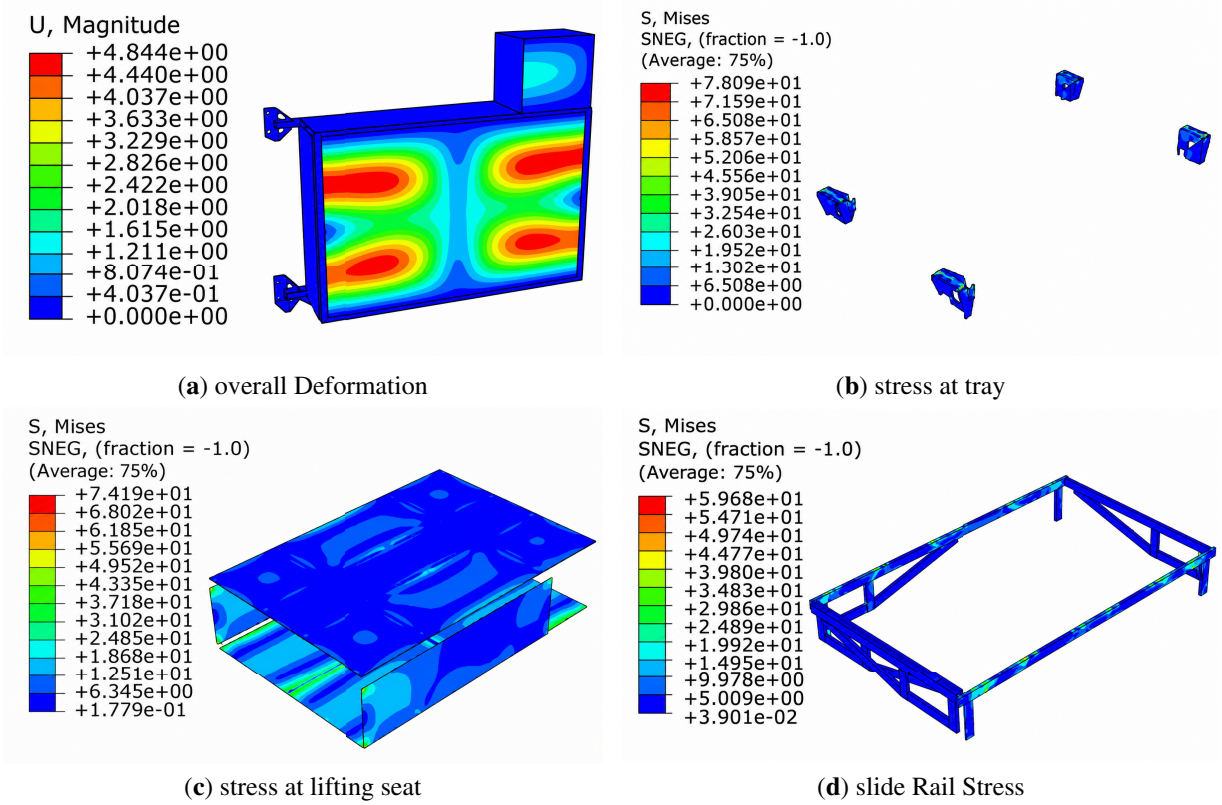

(**a**) overall Deformation (**b**) stress at tray

(**c**) stress at lifting seat (**d**) slide Rail Stress

Figure 7: Stress contours and deformation under static Condition 6 (−3 g vertical).

The maximum stress (186.6 MPa) occurs in the tray.

The detailed equivalent stress results and calculated safety factors for all components across all six static load cases are consolidated in Table 5. These findings align with prior studies on battery housing static performance [8].

Table 5: Equivalent stress results for static load conditions.

Condition	Component	Maximum Stress (MPa)	Yield Stress (MPa)	Safety Factor (Yield, ≥1.15)	Tensile Strength (MPa)	Safety Factor (Tensile, ≥1.5)
Condition 1	Lifting seat	115.7	205	1.8	515	4.5
	Frame	137.4	205	1.5	515	3.7
	Skin	72.23	205	2.8	515	7.1
	Outer panel	74.00	205	2.8	515	7.0
	Tray	184.7	205	1.1	515	2.8
	Slide rail	139.8	205	1.5	515	3.7
	Junction box	30.99	205	6.6	515	16.6

(Continued)

Table 5 (continued)

Condition	Component	Maximum Stress (MPa)	Yield Stress (MPa)	Safety Factor (Yield, ≥1.15)	Tensile Strength (MPa)	Safety Factor (Tensile, ≥1.5)
Condition 2	Lifting seat	119.3	205	1.7	515	4.3
	Frame	133.3	205	1.5	515	3.9
	Skin	70.96	205	2.9	515	7.3
	Outer panel	74.10	205	2.8	515	7.0
	Tray	175.6	205	1.2	515	2.9
	Slide rail	168.4	205	1.2	515	3.1
	Junction box	32.09	205	6.4	515	16.1
	Lifting seat	35.47	205	5.8	515	14.5
Condition 3	Frame	41.30	205	5.0	515	12.5
	Skin	27.36	205	7.5	515	18.8
	Outer panel	17.21	205	11.9	515	29.9
	Tray	70.46	205	2.9	515	7.3
	Slide rail	63.73	205	3.2	515	8.1
	Junction box	22.54	205	9.1	515	22.8
Condition 4	Lifting seat	32.21	205	6.4	515	16.0
	Frame	42.47	205	4.8	515	12.1
	Skin	27.99	205	7.3	515	18.4
	Outer panel	13.60	205	15.1	515	37.9
	Tray	70.08	205	2.9	515	7.3
	Slide rail	53.45	205	3.8	515	9.6
	Junction box	21.00	205	9.8	515	24.5
Condition 5	Lifting seat	78.09	205	2.6	515	6.6
	Frame	93.57	205	2.2	515	5.5
	Skin	74.19	205	2.8	515	6.9
	Outer panel	42.68	205	4.8	515	12.1
	Tray	186.6	205	1.1	515	2.8
	Slide rail	59.68	205	3.4	515	8.6
	Junction box	53.16	205	3.9	515	9.7
Condition 6	Lifting seat	78.09	205	2.6	515	6.6
	Frame	93.57	205	2.2	515	5.5
	Skin	74.19	205	2.8	515	6.9
	Outer panel	42.68	205	4.8	515	12.1
	Tray	186.6	205	1.1	515	2.8
	Slide rail	59.68	205	3.4	515	8.6
	Junction box	53.16	205	3.9	515	9.7

Key Finding: Under the most severe vertical ±3 g loads (Conditions 5 & 6), the tray was identified as the critical component, sustaining a maximum equivalent stress of 186.6 MPa. The corresponding safety

factor relative to the material yield strength is 1.1, which meets the DIN EN 12663 requirement (s_1 = 1.15, and s_2 = 1.5).

3.2 Fatigue Screening Results

To identify the critical components prone to fatigue failure, Fig. 8 illustrates the deformation patterns under selected load cases. Building upon this analysis, the maximum principal stress amplitudes were systematically evaluated. Fig. 9 provides a comparative overview of stress amplitudes among key components under the four loading conditions. The lifting seat and main frame consistently exhibit the highest stress amplitudes, reaching 39.38 and 37.87 MPa, respectively, under load case F3. By contrast, the outer skin and slide rail demonstrate significantly lower stress amplitudes (30.45 and 21.35 MPa, respectively). Such discrepancies can be attributed to the load transfer path: the lifting seat and main frame directly bear the battery weight and transmit inertial loads, whereas the outer skin and slide rail mainly act as protective and guiding structures with negligible load-bearing contributions.

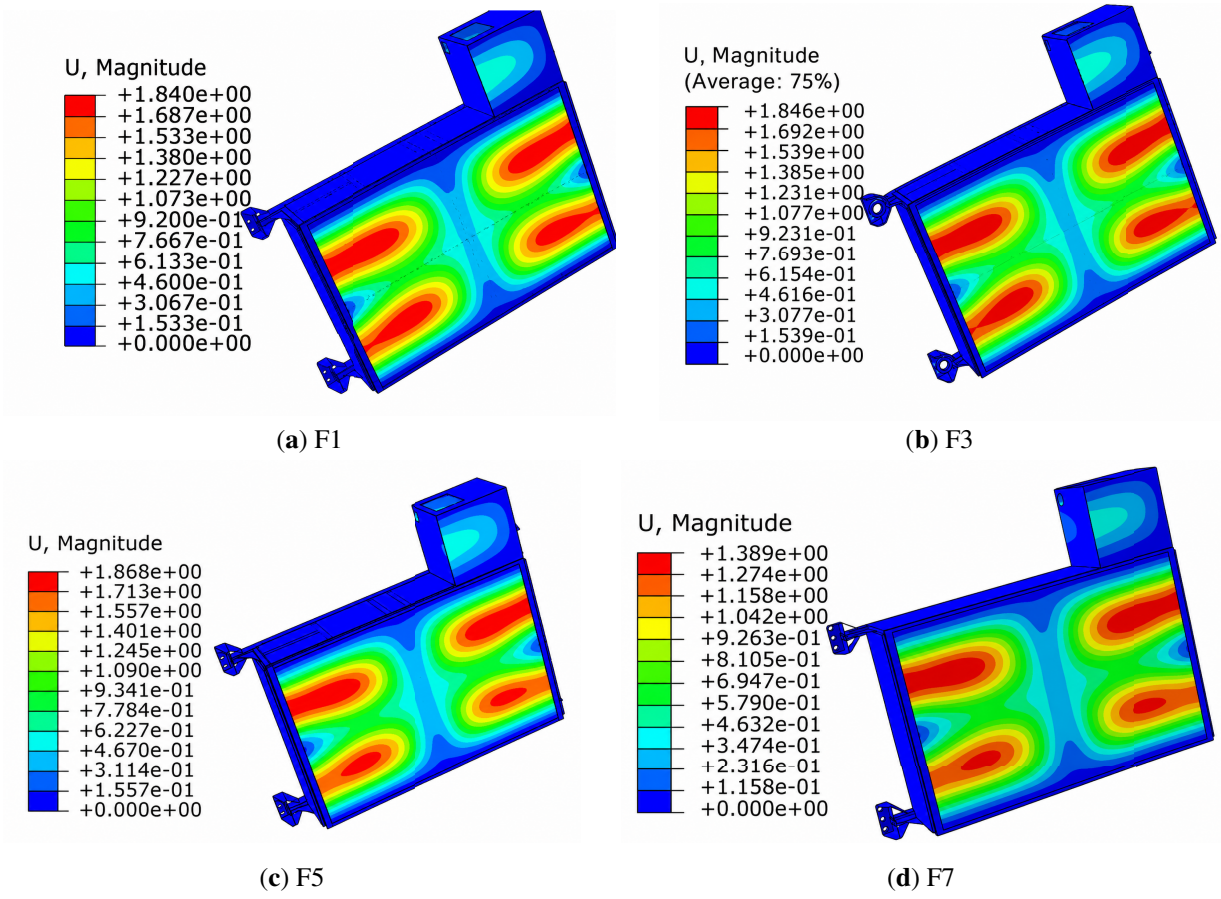

(**a**) F1 (**b**) F3

(**c**) F5 (**d**) F7

Figure 8: Comparison of deformation patterns under selected fatigue load cases (F1, F3, F5, F7).

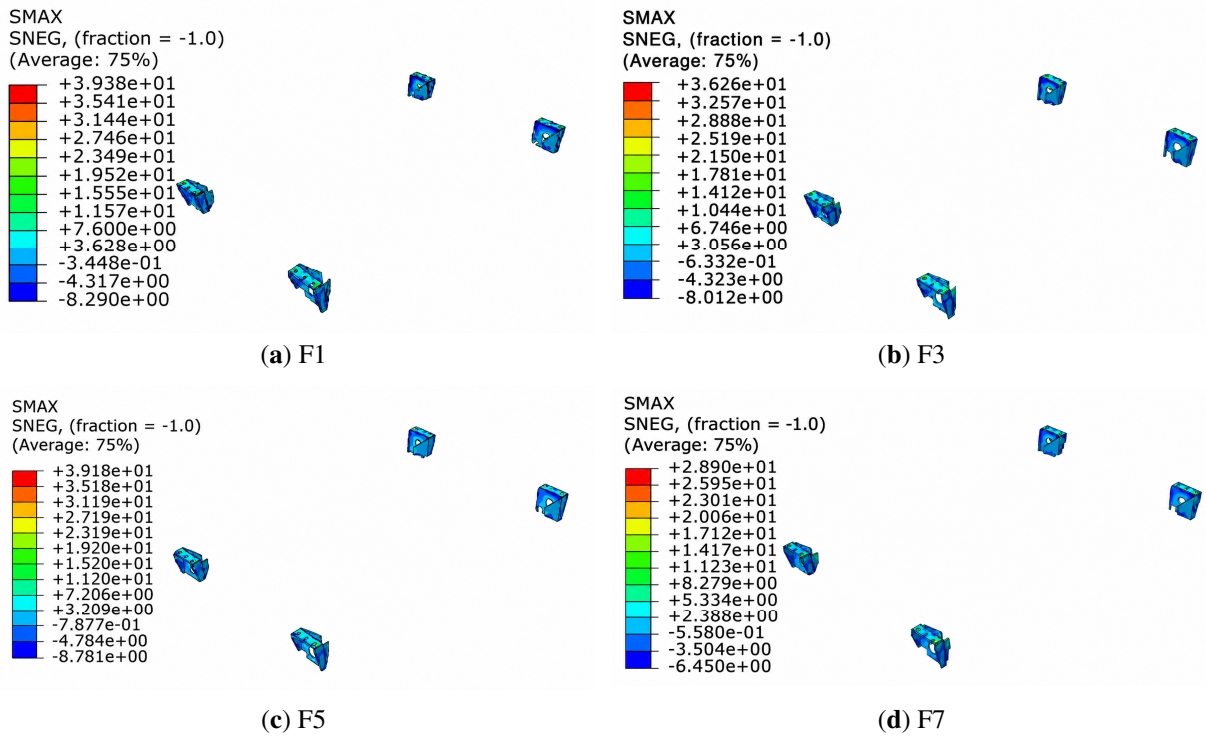

Figure 9: Maximum principal stress amplitude in the lifting seat under fatigue load spectrum (cases F1, F3, F5, F7). The maximum value is 39.38 MPa.

Under load case F3, the maximum principal stress amplitude in the lifting seat reaches 39.38 MPa, with stress concentration localized at the bolt-hole regions. This observation is consistent with the findings of Chen et al. [19], who performed experimental studies on train-induced vibrations in metro depot structures and reported that bolt-hole peripheries are particularly susceptible to multi-axial vibration excitation arising from track irregularities. In their field measurements, the combination of vertical and lateral vibrations induced by passing trains gave rise to amplified dynamic stresses at bolted connections—a phenomenon attributed to the superposition of bending and shear modes. While the present analysis adopts quasi-static load cases representing the extreme amplitudes of the fatigue spectrum (and thus does not explicitly capture resonance effects), the stress concentration pattern observed at the bolt holes aligns with the mechanism identified in [17]. This suggests that the quasi-static screening approach provides a conservative estimate of fatigue-critical locations.

Figs. 9–12 present the maximum principal stress contours for the main frame, lifting seat, outer skin, and slide rail, respectively. A comparative analysis reveals that while the deformation patterns are qualitatively similar across load cases F1–F8, the stress magnitudes differ significantly between components. The lifting seat (Fig. 9) and main frame (Fig. 9) consistently bear the highest dynamic loads, with stress peaks (e.g., 39.38 MPa) nearly 30% higher than those observed in the outer skin (Fig. 12). This differentiation justifies the individual focus on each component to ensure no localized fatigue risk is overlooked. Tables 6 and 7 summarize the maximum displacements under various static load conditions and the stress amplitudes as well as fatigue safety factors of the base material, respectively. The maximum static displacement reaches 4.844 mm under Conditions 5 and 6, whereas displacements under all fatigue load cases are considerably lower, ranging from 1.356 to 1.868 mm. Among fatigue conditions, the vertically dominated Cases 1 and 3 induce the largest deformations (approximately 1.85 mm), demonstrating that vertical loads dominate the global structural response.

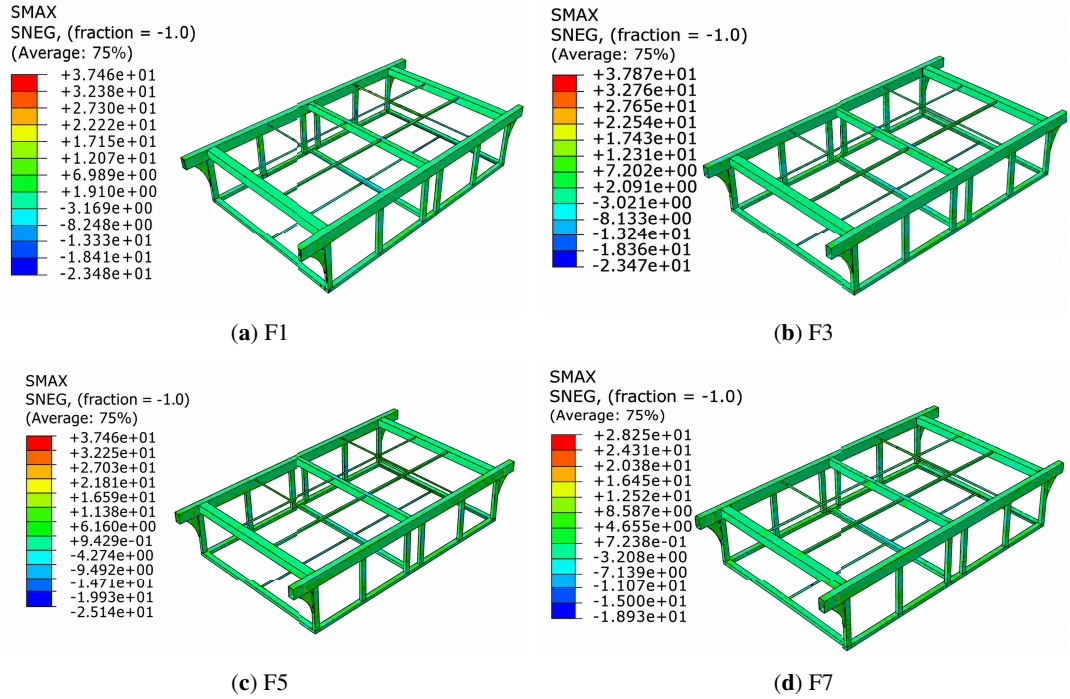

(**a**) F1 (**b**) F3

(**c**) F5 (**d**) F7

Figure 10: Maximum principal stress amplitude in the main frame under fatigue load spectrum (cases F1, F3, F5, F7). The maximum value is 37.87 MPa.

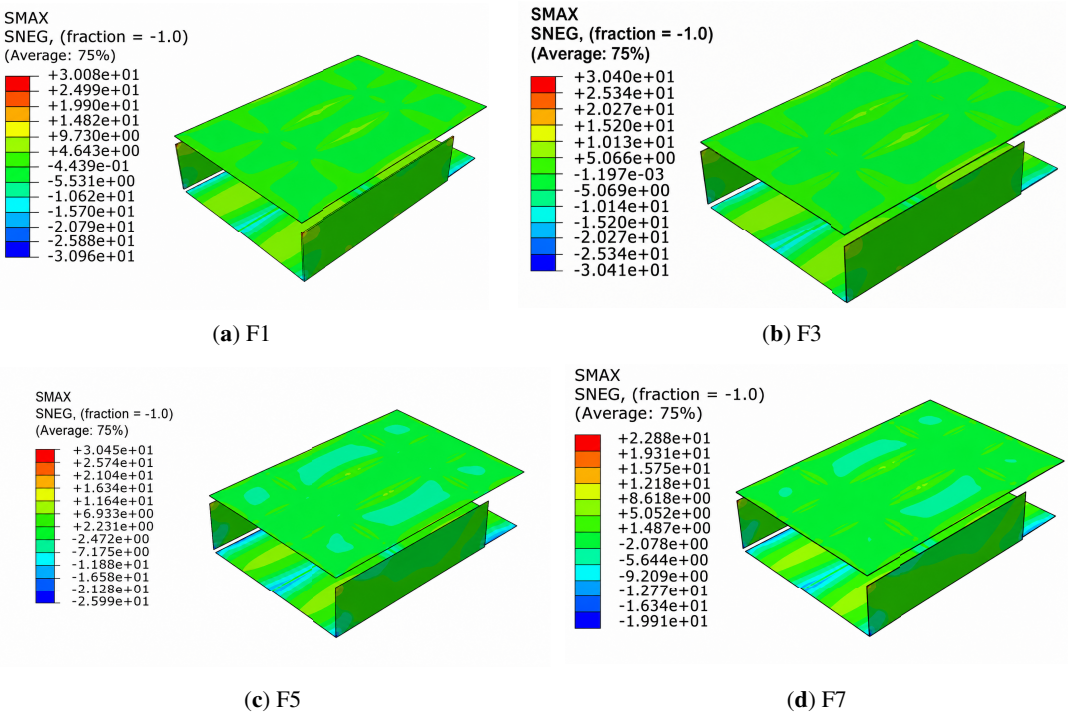

(**a**) F1 (**b**) F3

(**c**) F5 (**d**) F7

Figure 11: Maximum principal stress amplitude in the outer skin under fatigue load spectrum (cases F1, F3, F5, F7). The maximum value is 30.45 MPa.

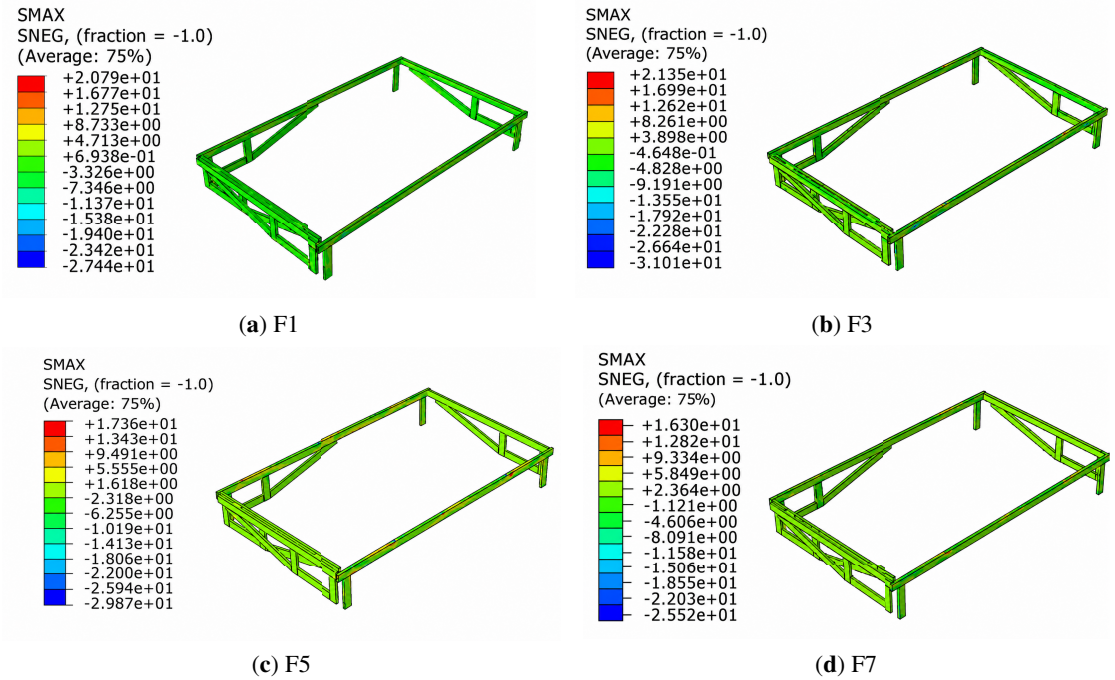

(**a**) F1 (**b**) F3

(**c**) F5 (**d**) F7

Figure 12: Maximum principal stress amplitude in the slide rail under fatigue load spectrum (cases F1, F3, F5, F7). The maximum value is 21.35 MPa.

Table 6: Displacement results (mm).

Static Load Condition	Deformation (mm)	Fatigue Condition	Deformation (mm)
Condition 1	2.431	Condition 1	1.840
Condition 2	2.594	Condition 2	1.356
Condition 3	1.618	Condition 3	1.846
Condition 4	1.636	Condition 4	1.362
Condition 5	4.844	Condition 5	1.868
Condition 6	4.844	Condition 6	1.389
/		Condition 7	1.389
		Condition 8	1.389

Table 7: Stress analysis results for base material fatigue conditions.

Location	Component	Maximum Stress Amplitude (MPa)	Sr (MPa)	Safety Factor (≥1.15)
Base material	Lifting seat	39.38	100	2.54
	Frame	37.87	100	2.64
	Skin	30.45	100	3.28
	Outer panel	10.80	100	9.3
	Tray	72.74	100	1.37
	Slide rail	21.35	100	4.68
	Junction box	23.88	100	4.19

According to the stress results presented in Table 7, the tray exhibits the highest stress amplitude of 72.74 MPa and the lowest safety factor of 1.37. Although this value remains above the required threshold of 1.15, it shows the smallest safety margin, identifying the tray as the most critical fatigue hotspot. The lifting seat and main frame display stress amplitudes of 39.38 and 37.87 MPa, with corresponding safety factors around 2.5–2.6, categorizing them as secondary load-bearing components. The skin, outer panel, slide rail, and junction box exhibit stress amplitudes below 31 MPa and safety factors significantly higher than the allowable limit (3.3–9.3), indicating negligible fatigue risk under cyclic loading.

Overall, all components meet the fatigue design criteria. Nevertheless, the tray requires particular attention, and it is recommended to alleviate its stress concentration by introducing stiffening ribs or optimizing the supporting boundary conditions.

3.3 Summary of Verification

The integrated analysis comprehensively verifies the structural reliability of the lightweight battery housing:

- Static Strength: All components satisfy the DIN EN 12663 standard, with the minimum safety factor of 1.1 found at the tray under extreme vertical loading.
- Fatigue Life: All critical locations exhibit stress amplitudes well below the allowable limit of BS 7608 Class B material, resulting in high fatigue safety factors (>2.5).
- System Performance: The coupled assessment confirms the integrity of bolted connections under operational cycling, validating the design against strength and fatigue failure modes.

4 Discussion

The implementation of the proposed "modelling-simulation-verification" framework yields critical insights into the coupled elastodynamic behavior of rail vehicle sub-assemblies, moving beyond traditional isolated component assessments.

4.1 Interpretation of Mechanical Response

The computational results reveal a distinct bifurcation in the governing failure mechanisms across the housing sub-components. Under static loading, the base tray emerges as the primary load-bearing element. Its mechanical response approximates that of a simply-supported plate subjected to the high inertial payload of the battery modules. During extreme vertical acceleration (±3 g), the tray undergoes a bending-dominated deformation, resulting in a peak von Mises stress of 186.6 MPa. In contrast, the lifting seat exhibits a heightened sensitivity to fatigue loading. The observed stress concentration (39.38 MPa) at the bolt-hole peripheries suggests a localized stress amplification mechanism. As noted in prior field investigations [17], multi-axial vibrations from track irregularities often trigger complex stress states at connection interfaces, where the resistance to cyclic loading is inherently lower than the static yield capacity. This discrepancy underscores the necessity of evaluating connection reliability independently of global structural strength.

4.2 Significance of the Integrated Method

This study addresses a pervasive limitation in contemporary rail vehicle engineering: the reliance on decoupled design workflows. Conventional practices typically evaluate global structural integrity and localized connection compliance in sequential, non-interactive stages. Such a methodology is fundamentally non-conservative; it risks overestimating structural capacity by neglecting the localized compliance of joints, or conversely, leading to mass-inefficient over-engineering by ignoring the stiffening effects of the

global assembly. The integrated framework proposed herein captures these critical interaction effects—specifically the redistribution of load paths and the formation of localized "hotspots" at fasteners—that are inherently obscured in decoupled analyses. By resolving the assembly-level mechanics, the framework ensures a physically representative evaluation of system-level reliability. Furthermore, by formalizing the verification process within the rigorous constraints of DIN EN 12663 and BS 7608, this research provides an audit-ready protocol for safety certification. This moves the state-of-the-art from *ad-hoc* simulation toward a standardized, standards-compliant methodology for coupled reliability assessment.

4.3 Engineering Contributions and Limitations of the Present Study

4.3.1 Engineering Contributions

The contributions of this work are dual-faceted:

(1) Methodological advancement: By bridging the analytical gap between global shells and localized beam-based bolt representations, the framework provides a computationally tractable solution for large-scale assembly screening. This addresses the research gap where housing structures and their connection systems are treated as separate mechanical entities.

(2) Design validation and transferability: The framework demonstrates that high-reliability, lightweight design is achievable through systematic procedural integration. The modular nature of the workflow—comprising parametric modelling, multi-condition spectra definition, and standard-based checking—is inherently transferable to other under-slung rail equipment, such as auxiliary power units or roof-mounted cooling modules, supporting broader industry efforts toward lifecycle standardization.

4.3.2 Limitations of the Present Study

While the proposed framework offers a robust tool for pre-service design verification, certain computational trade-offs were necessitated by the scale of the assembly. Bolted connections were abstracted using beam elements with tie constraints to maintain global convergence and efficiency. Consequently, highly localized phenomena—such as interface micro-slip, non-linear frictional dissipation, and thread-level contact mechanics—were not explicitly resolved. While omitted here to ensure the tractability of the global fatigue screening, these effects represent a logical transition from global reliability to localized joint physics.

Furthermore, the current analysis utilizes deterministic material parameters and load cases as mandated by industry standards [20]. Incorporating probabilistic distributions to account for manufacturing tolerances or stochastic track variations remains a vital direction for future reliability-centered design. Finally, while the FEA module is architecturally compatible with real-time sensor integration for digital twin applications, the present scope was strictly confined to initial design validation. These limitations define the boundaries of the current baseline and provide a clear trajectory for future research into uncertainty quantification and lifecycle health monitoring.

5 Conclusions

This study has successfully developed and applied an integrated "modelling-simulation-verification" framework for the reliability assessment of bolted connections in a lightweight (1000 kg) high-speed train battery housing. The principal findings are summarized as follows:

(1) Validation of Static Strength: Under the most critical vertical ±3 g static load conditions (per DIN EN 12663), the maximum equivalent stress occurs at the tray, reaching 186.6 MPa. The resulting minimum yield safety factor is 1.1, confirming compliance with the required standard ($s_1 \geq 1.15$) for all structural components (see Table 5, Fig. 7).

(2) Verification of Fatigue Performance: Under composite fatigue loading (per BS 7608), the lifting seat and the frame are identified as the most critical locations, sustaining maximum stress amplitudes of 39.38 and 37.87 MPa, respectively. The corresponding fatigue safety factors (2.54 and 2.64) substantially exceed the mandated threshold of 1.15, ensuring robust fatigue life (see Table 7, Figs. 9 and 10).
(3) System Reliability: The integrated analysis verifies the structural integrity and acceptable stiffness of the housing (maximum displacement: 4.844 mm) and the performance of bolted connections under multi-condition operational spectra, validating the design against both static and fatigue failure modes.

Acknowledgement: The authors acknowledge the financial support from Guangzhou College of Technology and Business.

Funding Statement: This research was supported by Guangzhou College of Technology and Business (University-Level Research Project, Grant No. KYZC202420) with the first author Lin Zang as principal recipient. Funding covered experimental materials, fatigue testing equipment usage, and open access publication fees. Project authenticity and funding allocation can be externally verified by contacting the university's Research Office at mail to: kyc@gzgs.edu.cn.

Author Contributions: Lin Zang conceived the research framework, developed experimental protocols, secured funding, and executed simulations. Muhammad Fadhil Marsani, Caiyan Long and Yongping Yu supervised project progress and refined manuscript quality through technical validation. All authors contributed to data analysis, algorithm feasibility evaluation, and collaborative writing. Final approval of the manuscript version was granted by Lin Zang, Muhammad Fadhil Marsani, Caiyan Long and Yongping Yu. All authors reviewed and approved the final version of the manuscript.

Availability of Data and Materials: The authors confirm that the data supporting the findings of this study are available within the article.

Ethics Approval: Not applicable.

Conflicts of Interest: The authors declare no conflicts of interest.

References

1. Yan F, Gong X, Luan P, Zhang W, Ren Y. Review of standards related to locomotive body strength. Railw Locomot Car. 2022;42(3):8–15.
2. Iwnicki S. Handbook of railway vehicle dynamics. Boca Raton, FL, USA: CRC Press; 2006. doi:10.1201/9780849333217.
3. Xiao X, Xu H, Yang Y, Chen P, Hua Q. Analysis of the influence of track irregularity on high-speed train ride comfort. Veh Syst Dyn. 2024;62(7):1658–85. doi:10.1080/00423114.2023.2250888.
4. Radaj D, Sonsino CM, Fricke W. Fatigue assessment of welded joints by local approaches. 3rd ed. Cambridge, UK: Woodhead Publishing; 2018.
5. Bickford JH. An introduction to the design and behavior of bolted joints. 4th ed. Boca Raton, FL, USA: CRC Press; 2007.
6. Duan G. New type sleeper train battery box static strength and fatigue strength analysis. China Equip Eng. 2016;13:2. doi:10.3969/j.issn.1671-0711.2016.13.046.
7. Lee YL, Pan J, Hathaway R, Barkey ME. Fatigue testing and analysis. Fatigue Fract Eng Mater Struct. 2005;28(12):987–95. doi:10.1016/B978-0-7506-7719-6.X5000-3.
8. Bannantine J. Fundamentals of metal fatigue analysis. 2nd ed. Upper Saddle River, NJ, USA: Prentice Hall; 1990. doi:10.5860/choice.27-2735.
9. Yang L, Chu M, Wang Q, Wang Z, Mo J. Dynamic response of high-speed train braking system under track irregularity excitation. J Mech Eng. 2025;61(24):281–92. doi:10.3901/JME.2025.12.281.

10. Zienkiewicz OC, Taylor RL. The finite element method: its basis and fundamentals. 7th ed. Oxford, UK: Butterworth-Heinemann; 2013.
11. Nassar S, Bickford JH, editors. Handbook of bolts and bolted joints. 2nd ed. Boca Raton, FL, USA: CRC Press; 2025. doi:10.1201/9781003501183.
12. Wang Y, Ma Y, Hong J, Battiato G, Firrone CM. Experimental studies on the energy dissipation of bolted structures with frictional interfaces: a review. Friction. 2024;12(3):457–89. doi:10.1007/s40544-023-0809-8.
13. Guo X, Tian D, Sun J, Zhang D, Liu Y, Zhang J. Evaluation of train-induced vibrations in medium-to-high speed railways: a parametric study. Front Built Environ. 2025;11:1577763. doi:10.3389/fbuil.2025.1577763.
14. Ma M, Xu L, Du L, Wu Z, Tan X. Prediction of building vibration induced by metro trains running in a curved tunnel. J Vib Control. 2020;27(5–6):515–28. doi:10.1177/1077546320930910.
15. Junker GH. New criteria for self-loosening of fasteners under vibration. SAE Trans. 1969;78:314–35. doi:10.4271/690055.
16. Li M, Ma M, Cao Z, Xia Q, Liu W. Dynamic response analysis of train-induced vibration impact on the Probhutaratna pagoda in Beijing. Earthq Eng Eng Vib. 2021;20(1):223–43. doi:10.1007/s11803-021-2016-9.
17. Zhai W, Wei K, Song X, Shao M. Experimental investigation into ground vibrations induced by very high speed trains on a non-ballasted track. Soil Dyn Earthq Eng. 2015;72:24–36. doi:10.1016/j.soildyn.2015.02.002.
18. Xia H, Zhang N, Cao YM. Experimental study of train-induced vibrations of environments and buildings. J Sound Vib. 2005;280(3–5):1017–29. doi:10.1016/j.jsv.2004.01.006.
19. Chen Y, Feng Q, Liu Q, Jiang J. Experimental study on the characteristics of train-induced vibration in a new structure of metro depot. Environ Sci Pollut Res Int. 2021;28(30):41407–22. doi:10.1007/s11356-021-13599-x.
20. DIN EN 12663-1:2010. Railway applications—structural requirements of railway vehicle bodies—part 1: locomotives and passenger rolling stock (and alternative rail vehicles). Berlin, Germany: Beuth Verlag; 2010. Standard withdrawn and replaced. Current version available from DIN National Standards Body.
21. Forcellini D, Kalfas KN. A framework to quantify the impact of deterioration on the seismic resilience of structures. Struct Infrastruct Eng. 2025:1–13. doi:10.1080/15732479.2025.2591824.
22. Kameshwar S, Forcellini D, Barbosa AR. Assessment of building recovery functions for local and global resilience assessment to tsunamis. Resilient Cities Struct. 2025;4:132–45. doi:10.1016/j.rcns.2025.10.001.